Breakup dynamics and the isotope effect in H_3^+ and D_3^+ dissociative recombination

D. Strasser,[1] L. Lammich,[2] H. Kreckel,[2] S. Krohn,[1,2] M. Lange,[2] A. Naaman,[1] D. Schwalm,[2] A. Wolf,[2] and D. Zajfman[1,2,*]
[1]*Department of Particle Physics, Weizmann Institute of Science, Rehovot, 76100, Israel*
[2]*Max-Planck-Institut für Kernphysik, D-69029 Heidelberg, Germany*
(Received 9 May 2002; published 25 September 2002)

The breakup dynamics of H_3^+ and D_3^+ following dissociative recombination is studied using the combination of two-dimensional imaging and storage ring techniques. The vibrational distributions of the molecular H_2 and D_2 fragments produced in the two body fragmentation channel were measured, as well as the kinematical correlation between the hydrogen or deuterium atoms produced in the three body channel. For the latter, we find predominantly linear dissociation geometries. The data also show that the initial molecular ions H_3^+ and D_3^+, which were stored and electron cooled for up to 40 s prior to recombination, are still rotationally hot.

DOI: 10.1103/PhysRevA.66.032719 PACS number(s): 34.80.Lx

I. INTRODUCTION

The triatomic hydrogen positive ion H_3^+ is the dominant molecular cation in a cold hydrogen plasma. As such, it plays an important role in diverse fields from chemistry to astronomy. Also, being the simplest polyatomic system, it finds much attention [1] as a benchmark system in quantum chemistry calculations for the treatment of polyatomic molecules in general. Regarding processes in ionized environments, in laboratory plasma tubes as well as in the cold interstellar medium, H_3^+ plays a central role by driving protonization reactions which in several steps lead to the formation of increasingly complex molecules [2]. In planetary science, H_3^+ is known to act as the dominant coolant of the Jovian ionosphere and is used for spectroscopic probing of the upper atmosphere of this planet [3].

Dissociative recombination (DR) is a neutralization process between a positive ion and a free electron, connected with a dissociation into neutral fragments. The DR of polyatomic ions plays an important role in many plasma environments, both as an ion destruction mechanism and as a pathway for the creation of smaller neutral molecules. In particular the DR of H_3^+, being the dominant destruction mechanism for this species in situations with significant electron densities, plays a critical role in models of the interstellar medium [4]. Thus a small uncertainty in the H_3^+ DR rate translates to a large uncertainty for the size of diffuse interstellar clouds, where H_3^+ infrared spectra have been measured [3].

The products of the DR of H_3^+ are either three neutral hydrogen atoms or a hydrogen molecule together with a hydrogen atom. For the most important case of near-zero initial energy, i.e., low-energy electrons and small internal excitation of the H_3^+ ion, the two reaction channels take the form

$$H_3^+ + e^-(E_e) \rightarrow \begin{cases} H(1s) + H(1s) + H(1s) & (\alpha) \\ H_2(X\,^1\Sigma_g^+, vJ) + H(1s) & (\beta). \end{cases} \quad (1)$$

The next electronically excited final channel, $H_2(X\,^1\Sigma_g^+, vJ) + H(n=2)$, opens when the initial energy exceeds ~ 1 eV. The situation for D_3^+ is largely equivalent, with small shifts of the relevant rovibrational level energies.

Despite intensive experimental [5] and theoretical [1] studies of the DR of H_3^+, the mechanism which drives the process is still far from being understood in its details and the DR rate coefficient is an issue of long-standing controversy. Laboratory measurements of the recombination cross section differ by four orders of magnitude [5]. The energy dependence of the cross section has been measured using the heavy ion storage ring technique at CRYRING [6], resulting in a rate coefficient of $\alpha = 1.15 \times 10^{-7}$ cm^3 s^{-1} for electrons at a temperature of 300 K. Two additional experiments at the storage rings ASTRID [7] and TARNII [8] have confirmed this value. The most recent reported values for the rate coefficient are from an experiment using the flowing afterglow technique, quoting a bound of $\alpha < 1 \times 10^{-8}$ cm^3 s^{-1} [9], in strong discrepancy with the storage ring results. Regarding more detailed properties of the DR reaction of H_3^+, the branching ratios for the two- and three-body channels (α) and (β) have been measured at CRYRING to be 25% and 75%, respectively [10].

Recently, we have studied [11] further dynamical aspects of the breakup process following the DR of H_3^+ using vibrationally relaxed ions in a storage ring. These measurements allow us to determine the vibrational excitation of the hydrogen molecular fragments produced in channel (β), as well as the kinematical correlations between the three hydrogen atoms in channel (α). Moreover, the observed total kinetic energy release indicates a very high, temporally stable rotational excitation of the stored H_3^+ ions, much stronger than in all other species for which similar storage-ring studies have been made earlier. This unexpected finding has already stimulated further storage ring measurements of the rate coefficient, performed with an ion source of a different type than previously and under various operating conditions, which reveal [12] an effect of the ion production mode on the measured DR rate and may thus signal an influence of the rotational excitation of H_3^+ on its DR rate coefficient.

*Author to whom correspondence should be addressed. Electronic address: fndaniel@wicc.weizmann.ac.il

In this work, we present a detailed account of our experiments on the breakup dynamics following the DR of triatomic hydrogen molecules, including an experimental comparison of the dissociation dynamics for the isotopomers H_3^+ and D_3^+. Data have been obtained on the energy sharing between the three dissociating fragments in channel (α) and on the vibrational population distributions of the molecular fragment in channel (β). Some emphasis is given to a detailed description of the data inversion procedure which allows us to extract the complete kinematical properties of the dissociation using a two-dimensional fragment imaging technique. Our data clearly display isotopic effects in the three-body dissociation dynamics and indicate that both H_3^+ and D_3^+ ions are rotationally hot before the DR.

II. EXPERIMENTAL SETUP

The experiments were carried out at the Test Storage Ring (TSR) located at the Max-Planck-Institut für Kernphysik, Heidelberg, Germany. The ring, which has already been used in several DR experiments (see, e.g., [13–17]), allows molecular ion beams to be stored with kinetic energies of a few hundred keV per atomic mass unit. In the present case, the H_3^+ (D_3^+) ions are produced in a ''hot'' gas discharge ion source, accelerated by a radio-frequency quadrupole accelerator to $v=0.032\,c$ ($v=0.016\,c$ for D_3^+), corresponding to a kinetic energy of 1.44 MeV (1.41 MeV), and injected into the storage ring. After each injection the ring (55.4 m circumference) typically holds about 10^6 ions, in an average vacuum of $\sim 3\times 10^{-11}$ mbar. At each pass, the ion beam is merged over a distance of 1.5 m with a cold collinear electron beam of equal mean velocity, which is produced by the electron cooler [18]. The electron beam is guided by a solenoidal magnetic field (field strength ~ 0.04 T) and steered in and out of the ring by toroidal magnetic field sections. Two settings of the electron beam parameters were used in the D_3^+ experiment, resulting in electron beam radii of 14.8 and 10.4 mm and electron densities of 3×10^6 and 6×10^6 cm^{-3}, respectively. In the H_3^+ experiment the electron beam radius was 21 mm and the electron density 3×10^6 cm^{-3}. The electron beam typically has a 0.1-meV longitudinal and a <25-meV transverse energy spread in the comoving reference frame.

During the first seconds of storage, the momentum spread of the ion beam is reduced by collisions with the cold electron beam (electron cooling), yielding a narrow beam with well defined transverse and longitudinal momentum, having a diameter of 0.8 mm for H_3^+ and 0.6 mm for D_3^+. This beam cooling is mandatory for our experiment as it ensures not only well defined relative energies between the electrons and ions [19] but also a well defined motion of the center of mass of the dissociation products in a plane perpendicular to the beam direction (see below).

Following the injection, the initially ''hot'' H_3^+ or D_3^+ molecular ions are given time to cool down by radiative relaxation. The vibrational relaxation of both H_3^+ and D_3^+ has been demonstrated previously using the Coulomb explosion imaging technique, and it was found [22] that the molecular ions are in their vibrational ground state after 3 s of storage for H_3^+ and after 6 s for D_3^+. However, since for both H_3^+ and D_3^+ rotational transitions between levels without vibrational excitation are forbidden, we do not expect the rotational degrees of freedom of the ions to thermalize with the blackbody radiation of the accelerator walls.

In the interaction region, where the ion and electron beams are merged, neutral fragments are produced in DR reactions. These fragments exit the ring and are detected using a two-dimensional (2D) imaging detector which is mounted straight ahead of the interaction region, at a distance of 6.47 m from the middle of the electron cooler. The 2D imaging detection scheme has been used extensively in the past years in various DR experiments (see, for example, Refs. [15,17]). The basic idea of the imaging method is to transform the momenta of the fragments released in the DR reaction into macroscopic (millimeter or even centimeter) distances on the detector plane and to measure the fragment impact positions event by event.

The 2D imaging setup consists of a microchannel plate (MCP) followed by a phosphor screen and a standard charge coupled device (CCD) camera. The impact of each particle on the MCP produces a light flash on the phosphor screen and the position of each impact is extracted by digitizing the image observed by the CCD camera. The detector is switched off about 1 μs after a hit has been detected on the detector. As this time is much shorter than the mean time between individual events ($\sim$ms), the camera mostly records only one single-molecule dissociation event (or background event) per frame. The detector is reactivated when the camera is ready to record another frame (typically after ~ 40 ms). The imaging detector can resolve multiple hits which are separated by more than 1 mm; its rms position resolution amounts to ~ 100 μm and the accuracy of the pixel-to-mm conversion factor is $\pm 0.9\%$. A more detailed description of the detector can be found in Ref. [16].

The use of the fragment imaging technique described above allows the correlations between all the fragments from the breakup of a single molecule to be recorded. These correlations can be exploited to obtain a superb signal-to-noise ratio as one can effectively discriminate against events which do not satisfy known kinematical properties, such as momentum conservation; on the other hand, one can probe unknown properties such as the underlying dynamics which govern the momentum correlations between the dissociating fragments.

III. THREE-FRAGMENT BREAKUP DYNAMICS

A. Energetics and data representation

When three ground-state hydrogen atoms are produced in the DR of H_3^+ or D_3^+, starting from an ion in its rovibrational ground state and with zero kinetic energy electrons [channel (α) in Eq. (1)], the total kinetic energy release (KER) E_k amounts to 4.76 or 4.63 eV, respectively. This energy can be shared between the dissociating atoms in many ways within the additional restrictions from momentum conservation, which, for example, limit the kinetic energy of any single fragment atom to $(2/3)E_k$. The energy

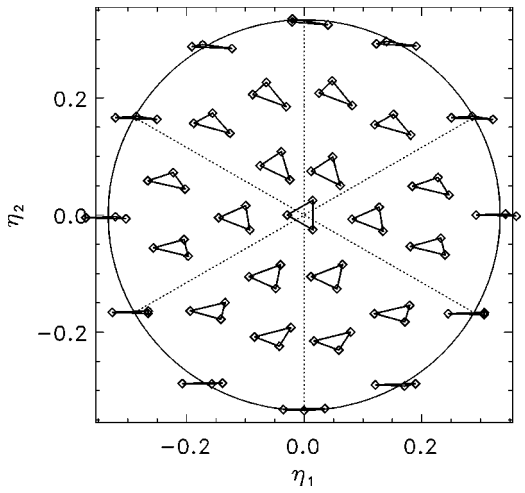

FIG. 1. Geometrical interpretation of the Dalitz plot using the coordinates from Eq. (2). The triangular shape corresponding to the respective coordinates is plotted for a sample of points in the (η_1, η_2) plane. The dashed lines and the circular boundary are discussed in the text.

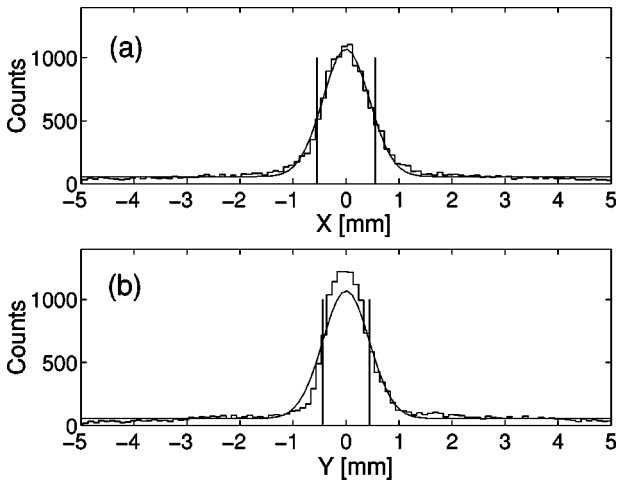

FIG. 2. Distributions of the center of mass position for three-hit events from the DR of D_3^+, as derived under the assumption of equal fragment masses; (a) horizontal and (b) vertical coordinate. The solid lines show Gaussian fits including a constant background; the windows of ± 1 standard deviation, used as c.m. cuts in the analysis, are indicated. The origins of the position scales were shifted to correspond to the centers of the fitted Gaussians.

sharing between the fragments uniquely determines the relative directions of the three momenta and hence the dissociation geometry, which is specified by the shape of the triangle spanned by the momentum vectors of the three fragments in the comoving frame of reference.

Using coordinates which are linear combinations of the single-particle kinetic energies E_i in the center-of-mass frame, the momentum correlation in three body systems can be represented in the two-dimensional Dalitz plot [20]. Preferred dissociation geometries, which are a manifestation of momentum correlations, appear as regions of enhanced density in distributions representing the geometries of a large number of dissociation events. The representation of such geometry distributions in a Dalitz plot offers the advantage that a uniform density indicates the absence of correlations, i.e., that the phase space is filled randomly under no further constraints than total momentum conservation. Keeping in mind that the systems considered here are invariant under exchange of fragments, the Dalitz coordinates η_1 and η_2 can be defined as

$$\eta_1 = (E_2 - E_1)/\sqrt{3}E_k,$$
$$\eta_2 = (2E_3 - E_2 - E_1)/3E_k \qquad (2)$$

with

$$E_k = E_1 + E_2 + E_3. \qquad (3)$$

For illustration, Fig. 1 shows representative cases of dissociation geometries distributed over the (η_1, η_2) plane, each point in this plane representing a unique dissociation geometry. Note that the momentum geometries of events at a given point of the histogram can have any overall orientation in space, and any overall size (as expressed by E_k). The sixfold symmetry under exchange of the fragment indices is marked by the three reflection axes (dashed lines). The circle drawn at $(\eta_1^2 + \eta_2^2)^{1/2} = 1/3$ gives the limitation imposed by energy and momentum conservation; this implies that the maximum energy carried by a single fragment has to be $\leqslant (2/3)E_k$. It is easy to identify the meaning of radius and angle, the polar coordinates in this representation, for the fragmentation geometry. Increasing radius in the (η_1, η_2) plane describes deformations from an equilateral shape towards linearity (found for points on the circumference of the momentum conservation circle). On the other hand, the angular coordinate in the Dalitz plot represents the symmetry—isosceles vs asymmetric—of the triangles.

As the 2D imaging technique records distances in the detector plane, transverse to the beam velocity, only transverse momenta and energies are measured. Through momentum conservation, the fragments' center of mass (c.m.) in the detector plane is determined by the initial motion of a dissociating molecular ion and the spatial distribution of the c.m. for many DR events reflects the transverse ion beam profile and its distribution of transverse velocities. As a consequence of the efficient electron cooling of the stored ion beam, yielding a small beam diameter and a small angular divergence, the c.m. positions of the DR events are localized within a narrow region of the detector plane. Figures 2(a) and 2(b) show typical c.m. distributions as measured for the x and y coordinates, respectively, for time-correlated three-hit events from D_3^+ DR. Our coordinate system is such that we define the z axis as being parallel to the beam velocity at the DR point and the x and y axes are parallel to the detector surface, the x axis lying in the plane defined by the structure of the storage ring, while the y axis is perpendicular to it. The c.m. coordinates are calculated from the three pairs of coordinates (x_i, y_i) measured for each event as

$$X=(x_1+x_2+x_3)/3,$$

$$Y=(y_1+y_2+y_3)/3. \quad (4)$$

The data shown in Fig. 2 were taken after 5 s of storage and cooling. Gaussian fits to the resulting c.m. distributions yield rms beam widths in the x and y direction of $\sigma_x=0.6$ mm and $\sigma_y=0.4$ mm, respectively. The difference between σ_x and σ_y is statistically significant and probably results from the different focusing structure for the horizontal and the transverse motion in the storage ring. To discriminate against random coincidences, only events for which the values of X and Y were less than one standard deviation away from the center of the distribution were accepted (see Fig. 2). Additionally, cuts with other acceptance windows for X and Y were used to check for possible effects of random coincidences and background events on the data.

Following a drift over the distance s from the dissociation point to the imaging detector, the transverse energy $E_{\perp i}$ of each fragment i in the c.m. frame can be directly obtained from its squared distance R_i^2 with respect to the center-of-mass position (X,Y), as measured on the surface of the imaging detector, using the relation

$$R_i^2 \equiv (x_i-X)^2+(y_i-Y)^2=(sv_{\perp i}/v)^2=3s^2E_{\perp i}/E_b. \quad (5)$$

Here $v_{\perp i}$ denotes the transverse velocity of fragment i in the c.m. frame, while v and E_b denote the velocity and the total kinetic energy of the dissociating molecule, as estimated from the ion beam velocity and the ion beam energy, respectively. In the same way

$$R^2 \equiv \sum_i R_i^2 = 3s^2E_\perp/E_b \quad (6)$$

determines the total transverse kinetic energy $E_\perp$.

We chose to represent the measured transverse fragment momentum geometry by ''transversal'' Dalitz coordinates Q_1 and Q_2 defined as

$$Q_1=(R_2^2-R_1^2)/\sqrt{3}R^2,$$

$$Q_2=(2R_3^2-R_2^2-R_1^2)/3R^2. \quad (7)$$

Similar to the (η_1,η_2) representation, each point in the (Q_1,Q_2) plane represents a single geometry of the three impact positions on the detector plane, which is in fact the projection of the (η_1,η_2) geometry in the dissociation plane onto the detector plane. However, there is no unique correspondence between the geometry in the dissociation plane and the projected geometry. Each specific dissociation geometry is transformed into a variety of different projected geometries, depending on the orientation of the dissociation plane. Nevertheless, as will be demonstrated in the next sections, it is possible to perform meaningful back-transformations of measured distributions in the (Q_1,Q_2) coordinates to momentum geometry distributions in the proper (η_1,η_2) Dalitz representation.

B. Monte Carlo simulation and response functions

Monte Carlo simulations were used to study the projection of dissociation geometries onto the detector plane. The simulation samples events with specific dissociation geometries (η_1,η_2), a given total energy release E_k, and with a *random* orientation of the dissociation plane. The events are generated taking into account the finite length of the interaction region in the electron cooler and translated to the imaging detector, finding the transverse coordinates R_i^2 and finally the corresponding coordinates in the (Q_1,Q_2) plot and the total transverse size R^2.

The assumption of a random, isotropic orientation of the dissociation plane is natural, since for zero kinetic energy electrons there is no preferable direction in space for this plane. Experimentally, this assumption has been verified in previous DR experiments on diatomics [16] and was always found to be valid for merged electron and ion beams with vanishing detuning between the average beam velocities. For triatomics, the isotropy can only be verified by true 3D imaging; for 2D imaging, effects of the dissociation geometry and, if existing, any anisotropy of the dissociation plane would be entangled in the total projected squared distance distribution for the three-body channel (Sec. III F). Taking into account the measured dissociation geometries, the three-body channel has a projected distribution very close to the isotropic distribution. For the two-body channel (Sec. IV B), the good fit over the main ascending part of the distribution excludes a strong anisotropy in the angular distribution.

Further experimental details were taken into account in various steps of the simulation. Thus, events were suppressed according to the fact that overlapping hits on the detector cannot be resolved if their distance is less than 1 mm. Moreover, the finite position resolution of the imaging detector was taken into account as an additional scatter on the impact positions x_i,y_i.

Figure 3 shows examples of distributions obtained in the (Q_1,Q_2) representation for specific dissociation geometries as given in the (η_1,η_2) representation. All samples are symmetrized with respect to the exchange of fragments in a final step of the simulation. We will refer to such projected distributions, calculated for single points in the (η_1,η_2) plane, as response functions, denoted by $S(Q_1,Q_2;\eta_1,\eta_2)$. In fact, the projection of any geometry distribution $F(\eta_1,\eta_2)$ onto the (Q_1,Q_2) plane can be described as the convolution with the response function S, according to

$$F^t(Q_1,Q_2)=\int S(Q_1,Q_2;\eta_1,\eta_2)F(\eta_1,\eta_2)\,d\eta_1 d\eta_2. \quad (8)$$

For each specific dissociation geometry the projected distribution is broadened but, as can be seen in Fig. 3, the peak location (Q_1,Q_2) nearly represents the original position (η_1,η_2). On the other hand, different points (η_1,η_2) have very different response functions, in particular with respect to the broadening effect. Thus, linear 3D geometries yield high and narrow peaks and geometries closer to an equilateral triangle yield lower and wider peaks. This is because the linear geometries have a higher symmetry: projection of a

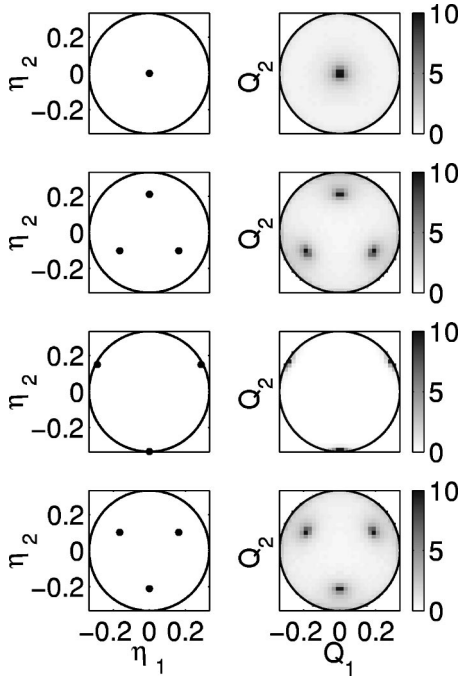

FIG. 3. Monte Carlo simulated and symmetrized projected geometry distributions (Q_1, Q_2 coordinates, right column) for selected fixed dissociation geometries (η_1, η_2 coordinates, left column). The (Q_1, Q_2) plots represent the response function $S(Q_1, Q_2; \eta_1, \eta_2)$ for the corresponding (η_1, η_2) geometry. All histograms shown here and below with a grayscale labeled by 0 to 10 are rescaled by an arbitrary factor to fit into this interval.

linear geometry onto a plane conserves the linear shape, while a projected triangular geometry is deformed and can even contribute linear geometries in the projected distribution. In fact, all initial geometries in the (η_1, η_2) space contribute at least to some degree to linear geometries after the projection; this creates a spurious maximum on the circumference of the limiting circle in the (Q_1, Q_2) plane for almost any initial distribution. The latter effect can be best observed in Fig. 4, which shows the projection of a random, uniform distribution in the (η_1, η_2) space to the (Q_1, Q_2) space; the enhancement at linear momentum geometries on the limiting circle is clearly the dominant feature in the projected distribution.

In spite of this strong distortion near the limiting circle of a projected distribution, the knowledge of the response function $S(Q_1, Q_2; \eta_1, \eta_2)$ helps in retrieving the characteristics of an original distribution $F(\eta_1, \eta_2)$ from measured data $F^t(Q_1, Q_2)$. A simple and straightforward method is to divide $F^t(Q_1, Q_2)$ by the projection $F^u(Q_1, Q_2) = \int S(Q_1, Q_2; \eta_1, \eta_2)\, d\eta_1 d\eta_2$ of a uniform (η_1, η_2) distribution (Fig. 4). This yields the weighted distribution

$$F^w(Q_1, Q_2) = \frac{F^t(Q_1, Q_2)}{\int S(Q_1, Q_2; \eta_1, \eta_2) d\eta_1 d\eta_2}, \qquad (9)$$

in which deviations from a uniform distribution of dissociation geometries are emphasized. Figure 5 shows how this

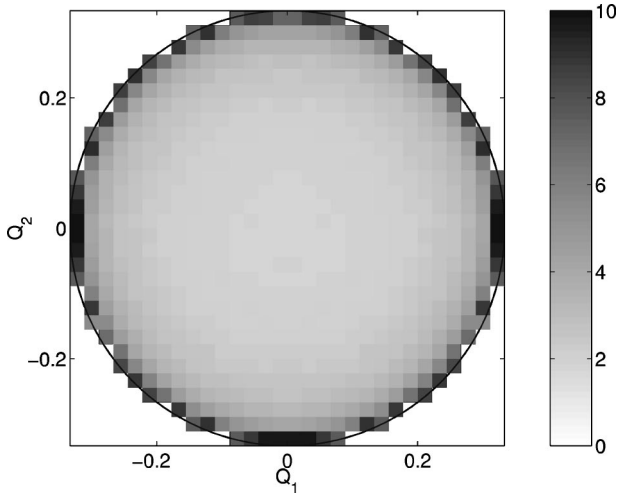

FIG. 4. Monte Carlo simulated and symmetrized projected geometry distribution for a uniform random distribution of dissociation geometries (η_1, η_2).

weighting scheme recovers the features of the original Dalitz plot for various initial momentum geometries. Three model distributions $F(\eta_1, \eta_2)$, in which different geometries are enhanced, are compared with their projections $F^t(Q_1, Q_2)$ and with the weighted distributions $F^w(Q_1, Q_2)$. Global features of the original distributions are in fact recovered by the weighting process, but they are considerably smeared out and the relative probabilities of different geometries cannot be reproduced by this method. This is to be expected as different dissociation geometries have very different response functions. Nevertheless, we use this straightforward and simple approach for a first interpretation of the measured projected momentum geometry distributions in the following section.

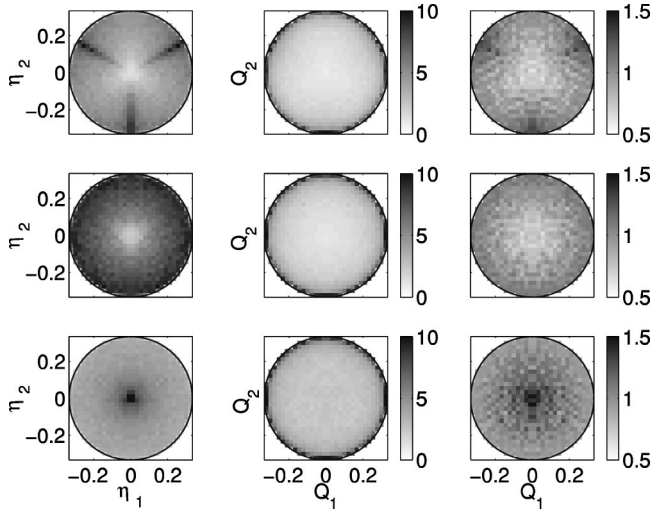

FIG. 5. Weighting scheme for projected momentum geometry distributions as applied to modeled dissociation geometry distributions. Left column: model distribution $F(\eta_1, \eta_2)$; center column: Monte Carlo simulated projected geometry distribution $F^t(Q_1, Q_2)$; right column: weighted projected geometry distribution $F^w(Q_1, Q_2)$ according to Eq. (9).

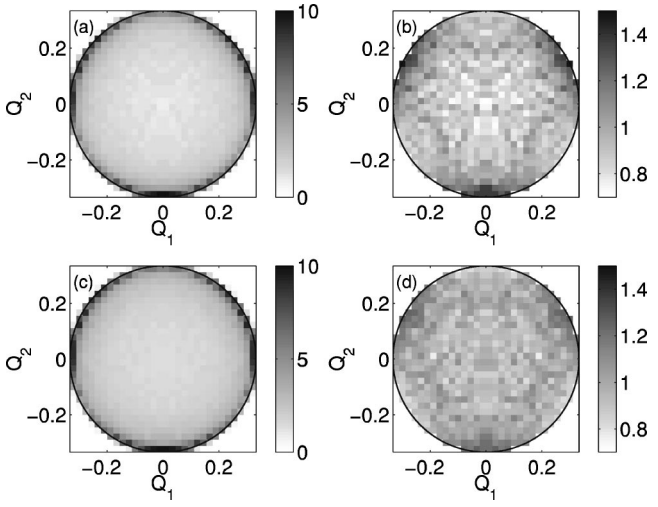

FIG. 6. Projected momentum geometry distributions measured for the DR of triatomic hydrogen ions. (a) Original and (b) weighted data for H_3^+; (c) original and (d) weighted data for D_3^+. The weighting applies Eq. (9) with the Monte Carlo simulated projection $F^u(Q_1,Q_2)$ of a uniform distribution (Fig. 4), scaled up to the same total number of events as in the corresponding measurement.

C. Experimental projected geometry distributions

Measured projected momentum geometry histograms $F^t(Q_1,Q_2)$ for H_3^+ and D_3^+ three-body fragmentation events and the corresponding weighted distributions $F^w(Q_1,Q_2)$ are displayed in Fig. 6. The experimental histograms presented in Figs. 6(a) and 6(c) contain 3.5×10^5 and 6.5×10^5 events, respectively. Both isotopomers show deviations from random dissociation in the weighted distributions, shown in Figs. 6(b) and 6(d). As was already stated for H_3^+ [11], colinear dissociation geometries are preferred (cf. Fig. 1). The weighted distribution for D_3^+ seems to display a smaller contrast between linear and triangular dissociation geometries than that of H_3^+. However, the strong smearing of the weighted projected distribution in comparison to the original 3D distribution, as demonstrated by the model calculations of Fig. 5, and the inability of the weighting scheme to give probability ratios for different momentum geometries make it difficult to draw more quantitative conclusions on possible isotope effects in the dissociation geometry of H_3^+ and D_3^+. We shall therefore turn to a more sophisticated data reconstruction technique which will allow the measured projected momentum distributions to be analyzed in more detail.

D. Monte Carlo reconstruction method

Three-dimensional (3D) momentum geometries cannot be recovered from 2D imaging data on an event-by-event basis. However, based on the assumption of an isotropic orientation of the dissociation plane, it is possible to obtain unique response functions $S(Q_1,Q_2;\eta_1,\eta_2)$ for the experimental projection transformation as described in Sec. III B and to reverse the projection described by Eq. (8), deconvoluting a measured histogram $F^t(Q_1,Q_2)$ in order to reconstruct the 3D momentum geometry distribution $F(\eta_1,\eta_2)$. We have calculated, using the Monte Carlo simulation described above, the response functions for 716 different dissociation geometries spanning the complete space of possible configurations (η_1,η_2). The deconvolution was then performed by implementing a Monte-Carlo image restoration technique (MCR). In this method [21], a representative distribution in the (η_1,η_2) space is built up from a large number of random trial events, which are selected by a set of well defined criteria in order to yield the best agreement with the measured 2D data after the transformation to the (Q_1,Q_2) space.

In detail, we divide the (η_1,η_2) and (Q_1,Q_2) spaces into bins x_n and y_m, respectively. The representative distribution of 3D dissociation geometries is constructed using the following procedure. To produce a single new entry in the representative histogram F^r in the (η_1,η_2) space, a large number N of candidate bins $\{x_n\}$ is chosen randomly ($N=200$ in our calculations). An initially empty cumulative distribution f^t is defined in the (Q_1,Q_2) space. If any bin x_n in the representative distribution F^r is incremented by one entry, the effect on f^t can be described by the replacement

$$f^t(y_m)\leftarrow f^t(y_m)+S(y_m;x_n), \tag{10}$$

according to the response function S. For each element out of the random sample $\{x_n\}$, the effect of this replacement is tested, finding the maximum value r of the ratio $f^t(y_m)/F^t(y_m)$ over all m, where $F^t(y_m)$ denotes the measured distribution. The particular bin x_p out of $\{x_n\}$ which produces the smallest value of r in this test is chosen as the new entry in F^r. The test can be efficiently programmed defining x_p as the choice that fulfills

$$f^t(y_m)\leqslant rF^t(y_m) \tag{11}$$

at all bins m with minimum r. After adding the entry by performing the replacement

$$F^r(x_p)\leftarrow F^r(x_p)+1, \tag{12}$$

the procedure is reiterated, filling more entries into F^r one by one. As customary for image reconstruction, in order to maintain the total intensity of an image [21], the MCR is stopped when the total number of events in the representative distribution $F^r(\eta_1,\eta_2)$ is equal to the number of events in the measured distribution $F^t(Q_1,Q_2)$. For infinite statistics, $F^r(\eta_1,\eta_2)\rightarrow F(\eta_1,\eta_2)$ since $f^t(Q_1,Q_2)\rightarrow F^t(Q_1,Q_2)$.

Before using the MCR technique to deconvolute our experimental results, we have tested the method by reconstructing different initially known distributions from their convolutions. Figure 7 compares some of the model distributions $F(\eta_1,\eta_2)$ to their reconstructions $F^r(\eta_1,\eta_2)$ obtained by the MCR technique, where model distributions were constructed with a number of events similar to those obtained experimentally (see Sec. III C). Also, the correct symmetry (under exchange of particle indices) was obtained by symmetrizing the accumulated representative distribution $F^r(\eta_1,\eta_2)$ at the end of the restoration process, using a suitable stochastic method to redistribute the bin contents. The MCR succeeds in recovering the different initial Dalitz plot

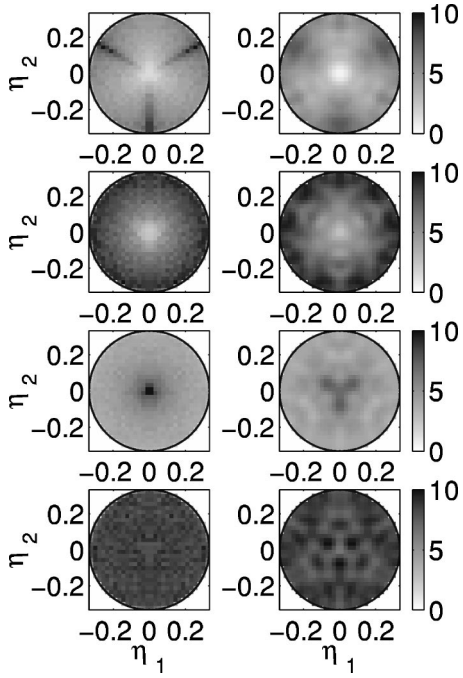

FIG. 7. Monte Carlo reconstruction of momentum geometry distributions from projected data, as applied to model distributions of dissociation geometries. Left column: model distribution $F(\eta_1,\eta_2)$; right column: representative distribution $F^r(\eta_1,\eta_2)$ as obtained by the Monte Carlo reconstruction of the simulated projected distribution $F^t(Q_1,Q_2)$ corresponding to $F(\eta_1,\eta_2)$. The lowest row is for a uniform distribution $F(\eta_1,\eta_2)$.

distributions in a way which, although not perfect, is more satisfactory than the outcome of the weighting method shown in Fig. 5, as the reconstructed histogram yields a considerably higher contrast which clearly reflects the relative probabilities in the original distribution. The most conspicuous difference between the original and the reconstructed distributions is the occurrence of additional smaller-scale fluctuations which we interpret as the ''noise patches'' that frequently arise in deconvolution processes; this can be seen most clearly for the case of a homogeneous model distribution $F(\eta_1,\eta_2)$ (last row of Fig. 7). Different arrangements of these patches occur for different statistical samples. The fluctuations of this type were found to be smoothed by the symmetrizing step at the end of the restoration, as the arrangement of the bins does not respect the underlying symmetry. However, the same operation also makes the noise patches occur in a regular pattern, a particularity that has to be taken into account when interpreting the deconvoluted distributions.

E. Experimental 3D reconstructed geometry distributions

Figure 8 shows the results of the MCR procedure for the momentum geometry distributions observed after DR of H_3^+ and D_3^+ into the three body fragmentation channel. These diagrams represent the MCR deconvolutions of the data in Figs. 6(a) and 6(c). As already stated in Ref. [11] for the case of H_3^+, a strong enhancement of colinear dissociation geometries (cf. Fig. 1) is found for both species. The enhancement is maximal around the symmetric configuration, where the central particle moves with the center of mass and the two other particles escape with equal but opposite momenta; on the other hand, dissociation geometries where two of the particles move with momenta close to each other are suppressed. This overall structure agrees with the weighted distributions shown in Figs. 5(b) and 5(d). However, two differences between H_3^+ and D_3^+ become more visible in the reconstructed distributions. First, while the H_3^+ data [Fig. 8(a)] show a dip in the center of the distribution, i.e., for the truly equilateral momentum geometries, this is not the case for D_3^+ [Fig. 8(b)]. Second, further out from the center the density rise towards the colinear symmetric momentum geometries is steeper in H_3^+ than in D_3^+. Although a more quantitative explanation of this isotope effect will have to wait until detailed quantum calculations of the dissociation dynamics become available, one might possibly understand this effect as a consequence of the different momentum distributions for the nuclei in the initial states of the two isotopomers. In the momentum space, the ground state wave function of the heavier D_3^+ isotope is broader than for H_3^+. Hence, because of the higher initial momentum, features in the D_3^+ momentum distributions observed after the dissociation may be expected to be less pronounced and more dispersed than for H_3^+.

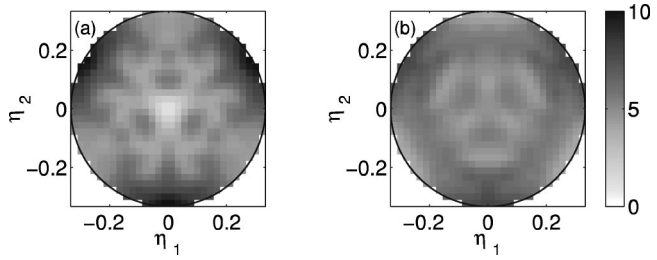

FIG. 8. Monte Carlo reconstructed momentum geometry distributions as obtained from the measured projected distributions shown in the left panels of Fig. 6 for (a) H_3^+ and (b) D_3^+.

F. Total projected squared distance distributions

Apart from the momentum geometry discussed in the previous sections, the observed three-fragment breakup events also yield information about the kinetic energy release (KER) of the DR reaction, as represented by the distributions of the (squared) total projected distance R^2 which was defined in Eqs. (5) and (6). In the full fragmentation channel [(α) in Eq. (1)] the KER is equal to the relative kinetic energy E_e of the electron plus the energy difference between the initial state of the molecular ion and the final state consisting of three dissociated atoms. At threshold, i.e., for $E_e=0$ and assuming that the molecular ions are in their rovibrational ground state, the KER is 4.76 eV for H_3^+ and 4.63 eV for D_3^+. As the 2D imaging technique records distances in the detector plane, transverse to the beam velocity, only the transverse part of the KER can be measured which, as pointed out above, is directly related to R^2 for a fixed distance s from the dissociation event to the detector. Figure 9 shows the measured R^2 distributions for the three-fragment

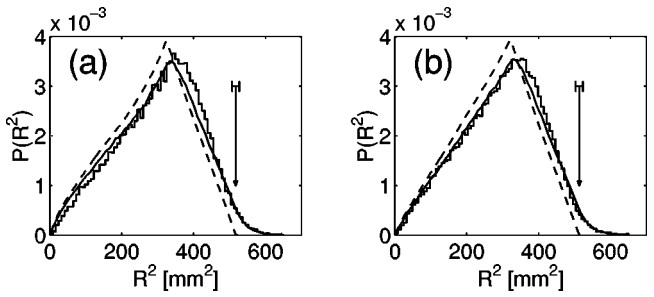

FIG. 9. Distributions of the total squared projected distance R^2 measured for the c.m.-cut three-hit events following the DR of (a) H_3^+ and (b) D_3^+. Also shown are Monte Carlo simulated distributions with the total kinetic energy of the fragments in the c.m. frame set to the threshold KER (dashed line) and to values given by the threshold KER plus a random excess energy from a Boltzmann distribution for an average energy of 0.3 eV (full smooth line). The expected end points of the R^2 distribution for the threshold KER (instrumental uncertainty of the end point position ± 10 mm^2) are indicated by the arrows.

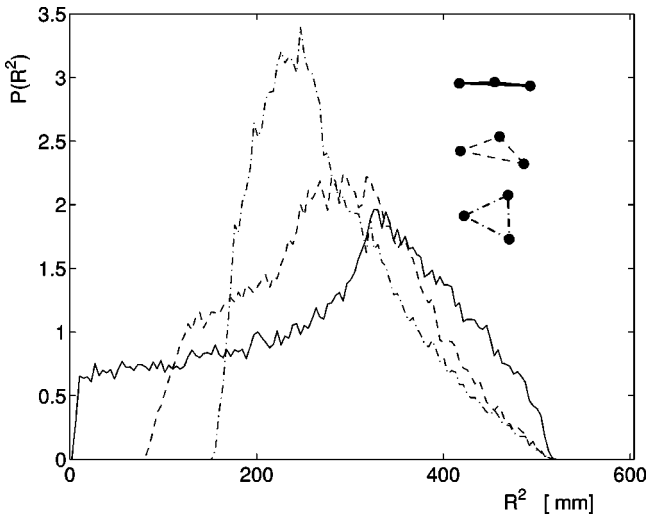

FIG. 10. Monte Carlo simulated R^2 distributions for the three-fragment breakup of H_3^+ for the threshold KER and three fixed dissociation geometries: almost linear [$(\eta_1, \eta_2) = (0,0.33)$; full line], flat triangle [$(\eta_1, \eta_2) = (0,0.16)$; dashed line] and equilateral triangle [$(\eta_1, \eta_2) = (0,0.02)$; dash-dotted line].

breakup channel of H_3^+ and D_3^+. The spectra were found to be independent of storage time from the end of the initial cooling-down period up to a maximum time of 40 s. The shape of the spectra reflects the distribution of the total transverse energy $E_\perp$, as indicated by Eq. (6), and in addition the scatter of the drift distance s due to the 1.5-m extension of the interaction region. Hence, events at the upper end point of the R^2 distribution correspond to those with the highest $E_\perp$ and the largest s.

In Fig. 9 the measured data are compared to the results of a Monte Carlo simulation, proceeding as described in Sec. III D but now extracting for the simulated events the total squared distance R^2 in the detector plane. Both for the experimental and the simulated data the histogram contents are normalized to the total number of events. The simulated distributions drawn by dashed lines were obtained assuming the threshold KER (i.e., cold molecular ions and zero electron energy) and a distribution of fragmentation geometries as given by the MCR of the experimental data for H_3^+ and D_3^+, respectively (Fig. 8). Figure 10 illustrates the effect of the dissociation geometry on the R^2 distribution. (It is interesting to note that all geometries with the same radius in the Dalitz plot have the same transverse energy distribution.) The measured data in Fig. 9 are close to the simulation in their overall shape; however, they appear to be shifted altogether by about 30 mm^2 towards higher R^2. Moreover, near the upper end point the experimental histograms not only are up-shifted with respect to the simulation, but also form a tail extending up to ~ 100 mm^2 beyond the simulated sharp end point.

Several experimental influences can be considered as possible origins of the up-shift and the tail of the measured distributions. First, including instrumental inaccuracies, the end-point positions of the R^2 distribution for the threshold KER can be predicted to be (517 ± 10) mm^2 and (513 ± 10) mm^2 for H_3^+ and D_3^+, respectively, the uncertainty appearing too small to explain the observed shift. Second, the experimental position resolution would be expected so smear out the measured R^2 distributions near the end point by only ± 17 mm^2, much less than the extension of the observed tails. In addition, we checked the possibility that these tails might be caused by random-coincidence background events by widening the limits for the c.m. cut explained in Sec. III A. We then obtained a much larger relative contribution of background events in the final data, but they formed an essentially flat baseline to the total R^2 distribution and did not change the relative intensity of the tail nor the shape of the histogram in the end-point region. We conclude that the discrepancies between the simulated and the measured R^2 distributions as well as the additional tail in the data are not a result of instrumental inaccuracies or random-coincidence background events, but rather reflect the presence of substantial excess energy in the dissociating systems (~ 0.3 eV for the average shift and up to ~ 1 eV for the tail).

Such an excess of energy can originate either from the relative kinetic energy E_e of the electrons or from an initial excitation of the H_3^+ and D_3^+ ions. The energy spread of the electron beam in the straight region of the electron cooler is only 25 meV, much smaller than the observed excess energies. Larger c.m. electron energies may be present for DR events taking place in the merging regions of the ion and the electron beam at both ends of the straight interaction zone. In these regions, where the electron beam is steered by toroidal magnetic fields, the c.m. electron energy rapidly increases from the meV values corresponding to parallel beams up to several 10 eV, corresponding to the maximum angles reached before the ion beam is completely steered out of the electron beam. Thus, sufficient excess energy would indeed be available within the merging regions, but this would affect only a minor fraction of all observed events because (1) the merging regions represent only a small part of the total overlap length and (2) for increasing electron energy E_e the recombination rate coefficient rapidly decreases [5], being reduced already by a factor of 10 for $E_e \sim 0.2$ eV. In contrast, the

comparison between the observed and the simulated distributions indicates that essentially all events are shifted up in R^2, the shift amounting on the average to $\sim 30\ \mathrm{mm}^2$ (roughly 0.3 eV) and in extreme cases (as reflected by the tails) up to $\sim 100\ \mathrm{mm}^2$ (roughly 1.0 eV). From the above arguments, the merging regions cannot upshift the KER for a large fraction of all observed events, and hence they cannot be at the origin of the observed effect. An additional experimental check of this conclusion is provided by the comparison of the two measurements performed for D_3^+ with different electron beam diameters (14.8 and 10.4 mm) and thus with somewhat different geometries in the merging and demerging regions; they did not show any change in the shape of the distribution, including the tail. Altogether, we find no explanation for the observed R^2 distributions in terms of excess energies provided by the interacting electrons.

On the other hand, excess energy for the reaction can also be provided by an initial excitation of the stored H_3^+ or D_3^+ ions, in the form of either vibrational or rotational energy. In this context, it is important to recall that the ions were stored for up to 10 s (H_3^+) or even 40 s (D_3^+) and that no significant changes of the R^2 distributions were observed following the initial cooling down period (3 s for H_3^+, 6 s for D_3^+). The vibrational excitation of H_3^+ and D_3^+ ions in the TSR as a function of cooling time was previously probed with the Coulomb explosion imaging (CEI) technique [22], which is sensitive to the vibrational but not the rotational excitation of the molecule. No changes of the nuclear position distributions measured by CEI were found in these experiments after the given initial cooling down times. In view of these results we are left with the conclusion that the observed excess energies are caused by an initial *rotational* excitation of the molecular ions. Such a conclusion is consistent with the fact that neither the H_3^+ nor the D_3^+ vibrational ground states have a permanent dipole moment, so that pure radiative rotational transitions are not allowed; hence, rotational cooling, if possible at all, is expected to be slow. Thus the rotational states excited in the production process of these molecular ions largely remain in the beam, with only small changes occurring through, e.g., rovibrational coupling.

We have performed a rough modeling of the effects due to an initial rotational excitation of the molecular ions by adding a Boltzmann-distributed excess energy of 0.3 eV on top of the expected threshold KER in the Monte Carlo simulation. The assumption of a Boltzmann distribution for the excess energy is highly simplifying because of two reasons: first, the energy distribution resulting from the production of the ions may be strongly nonthermal; and second, the size of the DR rate coefficient and also the dissociation geometry may strongly vary for different rotational levels. However, we restrict ourselves to this rough model since information which would enable us to include these expected dependencies in more detail is presently not available. The inclusion of rotational excitation (full lines in Fig. 9) considerably improves the agreement between the simulated and the measured R^2 distributions, although the measured shape, in particular between 400 and 500 mm^2, still cannot be completely reproduced. We consider the remaining deviations to be caused by the roughness of our model for the rotational excitation and by remaining uncertainties regarding the fragmentation geometry distributions; this would in particular affect the peak region of the R^2 histogram, as demonstrated by Fig. 10. On the other hand, the shape for lower R^2 and notably the tails near the upper end points are well accounted for by the modified simulation. We conclude from the ensemble of these arguments that both H_3^+ and D_3^+ are rotationally hot prior to DR, with an average rotational energy of ~ 0.3 eV.

The inferred rotational excitation, characterized by a Boltzmann distribution with the surprisingly high average energy of ~ 0.3 eV, can in fact be understood at least qualitatively. In a gas discharge ion source such as used here, H_3^+ ions are produced by the exothermic reaction of H_2^+ and H_2, which has an excess energy of 1.7 eV and therefore can lead to H_3^+ products with large angular momenta and large rovibrational excitation. In addition, already the electron bombardment of H_2 generates internally hot H_2^+ ions with typical vibrational excitations of several tenths of an eV, which also can contribute to a large rovibrational excitation of the H_3^+ ions formed in the $H_2^+ + H_2$ reaction. At the present ion source geometry it must be assumed that the ions are extracted before being able to thermalize with the surrounding plasma; hence, the molecular ions are certainly injected into the storage ring with a broad distribution of rovibrational states. During storage the ions can radiatively relax; however, the decay of rovibrational states is controlled by the dipole moment, which vanishes for rotational states with vibrational ground state character. As some of the vibrational modes do have a dipole moment that allows them to decay radiatively, the coupling between rotational and vibrational degrees of freedom can in principle induce some rotational relaxation even within the vibrational ground state. More detailed results of our CEI measurements regarding the vibrational relaxation times of H_3^+ and D_3^+ ions, which also indicate an influence of quasi-stable high-lying rotational states, will be given in a forthcoming publication.

IV. TWO-FRAGMENT BREAKUP DYNAMICS

A. Energetics and data representation

Two body fragmentation in the DR of H_3^+, considering the rovibrational ground state of the ion and zero-energy electrons, leads to an H atom in the $1s$ state and an H_2 molecule in state $^1\Sigma_g^+, vJ$ [case (β) in Eq. (1)] and a total energy of $E_t = 9.23$ eV is available to be shared between the rovibrational excitation of the H_2 product and the relative motion of the two fragments. The maximum rovibrational energy that can be stored in the molecular fragment is of the order of the H_2 dissociation energy of 4.48 eV. For D_3^+, the total available energy is $E_t = 9.19$ eV and the corresponding dissociation energy of the molecular product D_2 is 4.55 eV.

When the molecular ion dissociates into two fragments, two light spots are produced on the imaging detector. The center of mass is calculated from the two pairs of transverse coordinates measured for each event,

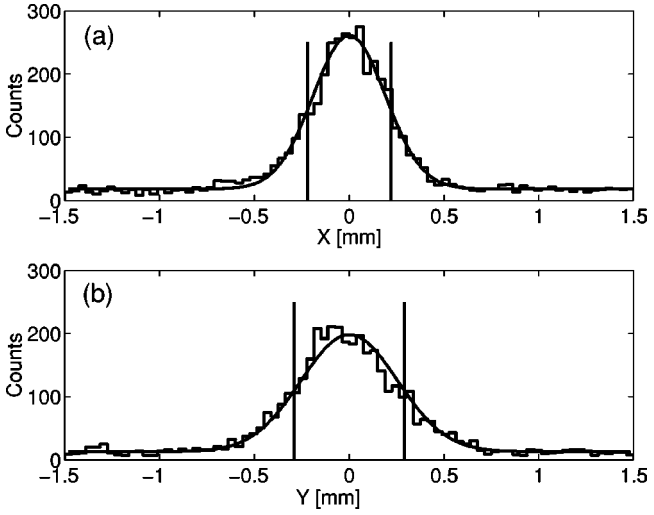

FIG. 11. Distributions of the center of mass position for two-hit events from the DR of D_3^+, as derived by assigning the molecular-fragment mass to the light flash closest to the c.m. position; (a) horizontal and (b) vertical coordinate. Gaussian fits and the limits of the c.m. cut are also shown; the origins of the position scales were shifted to correspond to the centers of the fitted Gaussians.

$$X=(2x_1+x_2)/3,$$

$$Y=(2y_1+y_2)/3. \tag{13}$$

The distributions of the c.m. position as observed for the two-hit events with D_3^+ are shown in Fig. 11. The signal due to two-body fragmentation is identified as a peak with the same position and width as that occurring for completely detected events in the corresponding three-hit distribution (Fig. 2); however, the two-hit events contain a larger background than the latter distribution, caused by three-body fragmentation events detected incompletely as a consequence of the finite detector efficiency ($\sim 50\%$). The c.m. cuts used to reduce the background are chosen to be the same as for the three-hit events. The coordinates (x_1,y_1) of the molecular fragment are identified as those of the light flash which is closer to the c.m. position of the respective event.

In order to obtain the vibrational distribution of the molecular fragments produced in the DR of H_3^+ or D_3^+, the projected distance distribution $P(D)$ between the two fragments was analyzed. Analysis of this type has already been described in detail for the DR of diatomic molecular ions [16]. In short, the projected distance distribution $P(D)$ with $D=[(x_1-x_2)^2+(y_1-y_2)^2]^{1/2}$ has a characteristic shape which depends on the geometry of the experiment and the KER. If a molecular fragment is produced in a vibrational state v with excitation energy E_v, the KER $E_{k,v}$ carried by the fragments is given by energy conservation as

$$E_{k,v}=E_t-E_v+\Delta E_{\mathrm{rot}}. \tag{14}$$

Here, ΔE_{rot} denotes the overall influence of rotational excitation in the initial H_3^+ ion and in the H_2 product molecule, as to be considered below. The functional form of the projected distance distribution between two fragments with relative kinetic energy $E_{k,v}$ is [16]

$$P^v(D)=\begin{cases}\dfrac{1}{\delta_v L}\left(\arccos\dfrac{D}{\delta_v s_2}-\arccos\dfrac{D}{\delta_v s_1}\right) \\ \quad \text{for } 0\leqslant D\leqslant \delta_v s_1, \\ \dfrac{1}{\delta_v L}\arccos\dfrac{D}{\delta_v s_2} \quad \text{for } \delta_v s_1\leqslant D\leqslant \delta_v s_2, \\ 0 \quad \text{otherwise,}\end{cases} \tag{15}$$

where s_1 and s_2 are the distances between detector and the downstream and upstream limits, respectively, of the straight interaction region in the electron cooler, $L=s_2-s_1$ is the interaction length, and δ_v is defined as

$$\delta_v=\frac{(m_1+m_1)}{\sqrt{m_1 m_2}}\sqrt{\frac{E_{k,v}}{E_b}}, \tag{16}$$

m_1 and m_2 being the fragments masses and E_b the beam energy. Since one out of several vibrational levels is populated in each individual dissociation process, the final projected distribution is given by a sum over all vibrational states as

$$P(D)=\sum_v P_v P^v(D), \tag{17}$$

where the (normalized) coefficients P_v represent the relative rates at which molecular fragments are produced in a given vibrational state v.

The vibrational state populations P_v can be deduced from a fit of the superposition according to Eqs. (15)–(17) to the data, using the constants P_v as free parameters and fixing the values of $E_{k,v}$ according to Eq. (14) for the respective v states. With the values of $E_{k,v}$ varying between ~ 9.2 eV for $v=0$ and ~ 4.7 eV for the highest H_2 product excitation, the end points of the different contributions $P_v(D)$ cover a considerable range (~ 10 mm) on the experimental D scale.

In comparison to the vibrational energies E_v, causing variations of the KER by several eV, the expected contributions to the KER expressed by ΔE_{rot} in Eq. (14) are rather small, even considering the relatively large degree of initial rotational excitation inferred for the stored H_3^+ and D_3^+ ion beams in Sec. III F. Moreover, the positive contribution to ΔE_{rot} due to the initial rotational excitation of the H_3^+ or D_3^+ ions may be compensated to some degree by rotational excitation energy carried away by the H_2 or D_2 products. Because of the limited capability of resolving contributions with different KER in our projected distance spectra, it is clearly out of reach for us to determine separately the size of the contributions with well defined initial and final J levels. Hence, our knowledge of the correction ΔE_{rot} remains limited; however, we can reasonably assume that ΔE_{rot} is small enough to allow the KER to be correlated to final v levels

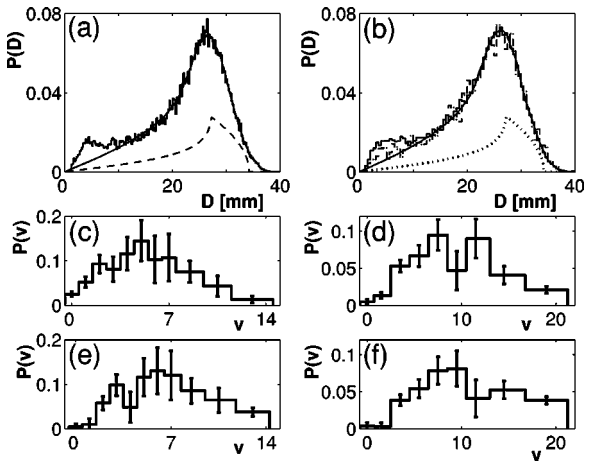

FIG. 12. Distributions of the projected distance D measured for the c.m.-cut two-hit events and derived vibrational population distributions of the molecular fragment. (a) Measured distribution $P(D)$ for H_3^+ (storage time interval 3–10 s) with a fitted sum of contributions $P^v(v)$ according to Eqs. (14)–(17) (full line) and a sample shape of a single-v contribution, shown for $v=5$ (dashed line); (b) measured distributions $P(D)$ for D_3^+ in the storage time intervals of 6–20 s (full histogram line) and 25–40 s (dashed histogram line) with a fit to the data for the early storage time interval (full line), and a sample shape for $v=9$. The correction $\Delta E_{\rm rot}$ due to rotational energies in the initial and final state is set to 0. Relative populations of different v states as obtained from these fits are shown for H_3^+ (c) and D_3^+ (d). In addition, vibrational populations obtained from fits with $\Delta E_{\rm rot}=0.3$ eV are shown for H_3^+ (e) and D_3^+ (f). For histogram bins spanning more than one unit in v, the relative populations were forced to be equal in the fit.

within about one unit of the quantum number (i.e., ± 1 in v), sufficient to obtain meaningful vibrational population distributions.

B. Results

Figure 12(a) shows the observed distribution $P(D)$ of projected distances D for H_3^+ in a measurement time window of $3<t<10$ s after injection. The result for D_3^+ in a time window of $6<t<40$ s after injection is shown in Fig. 12(b). In the data of Fig. 12 a background, mainly due to incompletely detected three-body fragmentation events, was subtracted. The shape of this background was obtained by finding the $P(D)$ distribution for measured events with a c.m. position outside the limits of the c.m. cut and its size was fitted to the high-D region of the c.m.-cut data. The procedure was tested using various limits for the c.m. cut, finding consistent spectra after the background subtraction.

The data of Fig. 12 were fitted for $D>10$ mm by superpositions of $P^v(D)$ distributions as described above, using $\Delta E_{\rm rot}=0$ in Eq. (14). A contribution $P^v(D)$ for one of the dominant v values is also shown. As can be seen the fits are perfect in the considered range $D>10$ mm. An equally good fit is obtained if $\Delta E_{\rm rot}$ is set to 0.3 eV. The first setting of $\Delta E_{\rm rot}=0$ assumes a situation where most of the initial rotational excitation of the H_3^+ ions is carried away by the H_2 products, while the second value ($\Delta E_{\rm rot}=0.3$ eV) accounts for the conclusions of Sec. III F and completely neglects any rotational excitation in the final H_2 molecules. For both choices of $\Delta E_{\rm rot}$ very similar v distributions are obtained, as shown in Figs. 12(c)–12(f).

For both H_2 and D_2, the deduced vibrational populations $P(v)$ are rather wide and basically all the vibrational states are populated. The populations peak around $v=5$ for H_2 and at $v=7$ to 8 for D_2. The shift of the most populated quantum states between the two isotopomers seems to reflect only the different vibrational level spacings of these species, while the distribution of vibrational energies given to the molecular fragment seems to be largely independent of the isotope for the two-body DR of H_3^+ and D_3^+.

The analysis so far was based on the data at transverse distances $D>10$ mm. Below this distance, a shoulder appears in the data which cannot be reproduced by any reasonable choice of fit parameters. The shoulder is found independent of the limits used in the c.m. cut and of the electron cooler configuration, as seen from comparing measurements with different electron densities and electron beam radii (see Sec. II). However, a significant dependence on the storage time of the ions is found for the size of the shoulder in the measurements with D_3^+, which could be extended up to 40 s after injection. Data for early and late storage time intervals (6–20 and 25–40 s, respectively) are compared in Fig. 12(b); the relative contribution of events within the shoulder (estimated from the ratio of the total number of counts in the histogram to the integral of the fitted function) is seen to decrease from $(5.8\pm 0.3)\%$ to $(2.4\pm 0.3)\%$ between the two storage time intervals.

Most likely, the shoulder is due to the presence of highly excited rotational states in the H_3^+ and D_3^+ ions before DR, as observed already in the three fragments channel (see Sec. III F). Very high lying rotational states with an energy of ~ 1 eV above the ground state can dissociate to the next available final-state channel $H(n=2)+H_2(^1\Sigma_g^+)$, which opens at an initial-state energy of 0.97 eV [or 1.01 eV for $D(n=2)+D_2(^1\Sigma_g^+)$]. Regarding the relative size of such additional contributions in the projected distance distribution, it is important to point out that it should depend not only on the relative population of rotationally excited states above the channel threshold, but also on the relative DR rate coefficient for the corresponding process. Involving highly excited initial levels as well as excited states of the atomic fragments, the invoked additional process can have a rate coefficient very different from that of the standard DR from low rotational states leading into the ground-state asymptotic channel; possibly, large values of the rate coefficient overemphasize the contribution from these highly excited states. This may also explain that a decrease due to extended storage times (and hence probably a radiative relaxation) can be observed for the shoulder in the two-body fragmentation data [Fig. 12(b)], while the energy release spectra for the three-body breakup channel (Fig. 9) show no significant time variation. Thus the shoulder in the two-body projected distance distribution can probably be attributed to a small population of very highly excited initial rotational levels, while the same highly excited levels yield only a negligible contri-

bution to the three-body breakup channel. In any case, even for the very highly excited levels considered to cause two-body breakup events with hydrogenic $n=2$ final states, any relaxation appears to proceed on a very long time scale only.

V. DISCUSSION AND CONCLUSIONS

The data presented here for the two- and three-body fragmentation channels in the DR of H_3^+ and D_3^+ can be compared to experimental results and theoretical predictions regarding the predissociation of single rovibrational Rydberg states of H_3. Geometry distributions for the predissociation of several well defined rovibrational Rydberg states of H_3 have recently been measured by Müller *et al.* [23]. A comparison with these results appears to be of interest since largely the same electronic potential surfaces can be assumed to be responsible for the predissociation of H_3 Rydberg states as for the DR of H_3^+.

For the predissociation case, the experimental momentum correlation spectra were found to be highly structured and very sensitive to the initial state symmetry, a feature which was attributed to differences in the coupling mechanisms with the dissociative states. In contrast, the geometry distributions obtained here (see Fig. 8) are not as structured, although existing details might partly be washed out by the reconstruction process. The lack of structure may be explained on the one hand by intrinsic properties of the DR process, where a large number of symmetries can be realized in the initial state and no quasi-stable initial states exist. On the other hand, our DR data indicate that a large number of initial rotational states are populated in the H_3^+ and D_3^+ ions, which may average out any more detailed structures in the geometry distributions for the DR of ions in well-defined rotational states. Future DR measurements with rotationally cold molecular ions are needed to clarify this point.

Regarding the predominance of the linear dissociation, reasons based on a simple physical picture have already been suggested in Ref. [11]. These arguments referred to the two possible spin configurations between the different H–H pairs, which puts one pair into a triplet (and hence repulsive) configuration, while the two other pairs form singlets (attractive, or less repulsive). Under a theoretical point of view, a comparison between the data obtained here and wave-packet calculations performed for the predissociation of H_3 can be made. In a two-dimensional calculation (restricted to the isosceles, C_{2v} geometry) using diabatic potential surfaces, a predominance of linear fragmentation was found for the three-body channel [25], while a later calculation [26] without the geometrical restriction, but using adiabatic potential surfaces, found a predominance of triangular structures. Our data rather agree with the result of the first calculation [25], but as these calculations are limited to two dimensions, care should be taken in judging the validity of the underlying theoretical approaches on this basis. Obviously more detailed calculations are needed.

For the two-fragment channel, the vibrational state distributions obtained here provide quantitative evidence about the excitation of the molecular fragment. In comparison to related results for the predissociation of $n=3$ Rydberg states in H_3 [24], the present fragment state distribution is found to be even wider. It may be useful to note that also the total energy available for the dissociation is larger in the DR case than in the predissociation case.

As we already reported for H_3^+, a statistical model for calculating DR branching ratios [27] can reproduce the vibrational state distributions of the molecular fragment in both H_3^+ and D_3^+ DR in good agreement with the measured results. Also, a recent *ab initio* calculation [1] for the DR of H_3^+ is in accord with the peak location of the measured vibrational distribution.

An additional important conclusion from the results given above is that it should be carefully considered whether the experiments so far performed in storage rings on the DR of H_3^+ and D_3^+, in particular the rate coefficient measurements of Refs. [6–8], might possibly have used rotationally excited species in a similar way as in the present arrangement. In fact, as pointed out in Sec. I, preliminary recent storage-ring results [12] indicate that the absolute rate coefficient measured after substantial storage times is still influenced by the ion source conditions, which might be related to the initial rotational distribution of H_3^+. We also propose to check if the large disagreements existing between the different experimental values for the DR of the triatomic hydrogen ion are not due to the different initial rotational populations produced in the various environments. While we did not measure the absolute DR rate coefficient for H_3^+ or D_3^+ in our experiments, it cannot be excluded that also the specific dynamical properties of the DR process studied here are strongly affected by the inferred large rotational energies of the stored ions.

ACKNOWLEDGMENTS

This work has been funded in part by the German Federal Minister for Education, Science, Research and Technology (BMBF) within the framework of the German-Israeli Project Cooperation in Future-Oriented Topics (DIP) and by the European Community's Research Training Networks Program under Contract No. HPRN-CT-2000-0142, ETR.

[1] V. Kokoouline, C.H. Green, and B.D. Esry, Nature (London) **412**, 891 (2001).
[2] E. Herbst and W. Klemperer, Astrophys. J. **185**, 505 (1973).
[3] B.J. McCall and T. Oka, Science **287**, 1941 (2000).
[4] S. Lepp, Nature (London) **366**, 633 (1993).
[5] M. Larsson, Philos. Trans. R. Soc. London, Ser. A **358**, 2433 (2000).
[6] G. Sundström *et al.*, Science **263**, 785 (1994).
[7] M.J. Jensen *et al.*, Phys. Rev. A **63**, 052701 (2001).
[8] T. Tanabe, in *Dissociative Recombination: Theory, Experiment*

and Applications IV, edited by M. Larsson, J. B. A. Mitchell, and I. F. Schneider (World Scientific, Singapore, 2000), p. 170.
[9] J. Glosik *et al.*, J. Phys. B **34**, L485 (2001).
[10] S. Datz *et al.*, Phys. Rev. Lett. **74**, 896 (1995).
[11] D. Strasser *et al.*, Phys. Rev. Lett. **86**, 779 (2001).
[12] M. Larsson (private communication).
[13] P. Forck *et al.*, Phys. Rev. Lett. **70**, 426 (1993).
[14] P. Forck *et al.*, Phys. Rev. Lett. **72**, 2002 (1994).
[15] D. Zajfman *et al.*, Phys. Rev. Lett. **75**, 814 (1995).
[16] Z. Amitay *et al.*, Phys. Rev. A **54**, 4032 (1996).
[17] Z. Amitay *et al.*, Science **281**, 75 (1998).
[18] D. Habs *et al.*, Nucl. Instrum. Methods Phys. Res. B **43**, 390 (1989).
[19] G. Kilgus *et al.*, Phys. Rev. A **46**, 5730 (1992).
[20] R.H. Dalitz, Philos. Mag. **44**, 1068 (1953).
[21] B. R. Frieden, in *Picture Processing and Digital Filtering*, Vol. 6 of *Topics in Applied Physics*, edited by T. S. Huang (Springer-Verlag, Berlin, 1975), p. 177.
[22] H. Kreckel, diploma thesis, University of Heidelberg, 2000.
[23] U. Müller, T. Eckert, M. Braun, and H. Helm, Phys. Rev. Lett. **83**, 2718 (1999).
[24] U. Müller and P.C. Cosby, J. Chem. Phys. **105**, 3532 (1996).
[25] A.E. Orel and K.C. Kulander, J. Chem. Phys. **91**, 6086 (1989).
[26] J.L. Krause, K.C. Kulander, J.C. Light, and A.E. Orel, J. Chem. Phys. **96**, 4283 (1992).
[27] D. Strasser *et al.*, Phys. Rev. A **65**, 010702 (2002).